JACS
ARTICLES
Published on Web 05/20/2006

Nickel Superoxide Dismutase Reaction Mechanism Studied by Hybrid Density Functional Methods

Vladimir Pelmenschikov*,† and Per E. M. Siegbahn

Contribution from the Department of Physics, Stockholm University, SE-106 91, Stockholm, Sweden

Received June 3, 2005; E-mail: vovan@physto.se

Abstract: The reaction mechanism for the disproportionation of the toxic superoxide radical to molecular oxygen and hydrogen peroxide by the nickel-dependent superoxide dismutase (NiSOD) has been studied using the B3LYP hybrid DFT method. Based on the recent X-ray structures of the enzyme in the resting oxidized Ni(III) and X-ray-reduced Ni(II) states, the model investigated includes the backbone spacer of six residues (sequence numbers 1−6) as a structural framework. The side chains of residues His1, Cys2, and Cys6, which are essential for nickel binding and catalysis, were modeled explicitly. The catalytic cycle consists of two half-reactions, each initiated by the successive substrate approach to the metal center. The two protons necessary for the dismutation are postulated to be delivered concertedly with the superoxide radical anions. The first (reductive) phase involves Ni(III) reduction to Ni(II), and the second (oxidative) phase involves the metal reoxidation back to its resting state. The Cys2 thiolate sulfur serves as a transient protonation site in the interim between the two half-reactions, allowing for the dioxygen and hydrogen peroxide molecules to be released in the reductive and oxidative phases, respectively. The His1 side chain nitrogen and backbone amides of the active site channel are shown to be less favorable transient proton locations, as compared to the Cys2 sulfur. Comparisons are made to the Cu- and Zn-dependent SOD, studied previously using similar models.

I. Introduction

Superoxide dismutases (SODs, EC 1.15.1.1) are metalloenzymes that catalyze the disproportionation of superoxide to molecular oxygen and hydrogen peroxide:

$$2O_2^{\bullet -} + 2H^+ \xrightarrow{\text{SOD}} O_2 + H_2O_2 \qquad (1)$$

Generated by a single-electron transfer to dioxygen, superoxide radicals are produced in large amounts in respiration and photosynthesis, during an immune response by phagocytes, etc.[1,2] SODs play an important protective role in aerobes which encounter toxic $O_2^{\bullet -}$ radicals during their metabolism. The presence of SOD in the intracellular environment reduces oxidative stress and can play a key role in moderating the aging process. SOD is therefore used as an antioxidative therapeutic agent. Other medical applications involve treatment of arthritis and prevention of side effects of cancer treatment and injury to transplant organs during surgery. Given that mutations in SOD are associated with 20% of the cases of familiar amyotrophic lateral sclerosis (FALS),[3−6] the enzyme is used to block the development of this paralytic disorder.

To date, three independent SOD classes are known, classified based on their cofactor metal ion: Cu- and Zn-dependent SODs (CuZnSODs), SODs that use Fe or Mn, or either of the two (FeSODs, MnSODs, or Fe/MnSODs), and Ni-dependent enzymes (NiSODs). While CuZnSODs are the most abundant superoxide scavengers in living nature, found in all eucaryotes and many procaryotes,[7] the recently discovered NiSOD class is confined to *Steptomyces* soil bacteria[8−10] and cyanobacteria.[11] Extending the short list of Ni-dependent enzymes,[12] the novel class of SOD was initially reported to function as a homotetramer.[8−10,13] However, the latest X-ray crystallographic structure

† Present address: Department of Molecular Biology, TPC15, The Scripps Research Institute, 10550 North Torrey Pines Road, La Jolla, CA 92037.

(1) Fridovich, I. *J. Biol. Chem.* **1989**, *264*, 7761−7764.
(2) Fridovich, I. *J. Exp. Biol.* **1998**, *201*, 1203−1209.
(3) Rosen, D. R.; Siddique, T.; Patterson, D.; Figlewicz, D. A.; Sapp, P.; Hentati, A.; Donaldson, D.; Goto, J.; O'Regan, J. P.; Deng, H. X. *Nature* **1993**, *362*, 59−62.
(4) Orrell, R. W. *Neuromuscular Disord.* **2000**, *10*, 63−68.
(5) Stathopulos, P. B.; Rumfeldt, J. A.; Scholz, G. A.; Irani, R. A.; Frey, H. E.; Hallewell, R. A.; Lepock, J. R.; Meiering, E. M. *Proc. Natl. Acad. Sci. U.S.A.* **2003**, *100*, 7021−7026.
(6) Liochev, S. I.; Fridovich, I. *Free Radical Biol. Med.* **2003**, *34*, 1383−1389.
(7) Bordo, D.; Pesce, A.; Bolognesi, M.; Stroppolo, M. E.; Falconi, M.; Desideri, A. In *Handbook of Metalloproteins*, Messerschmidt, A., Huber, R., Poulos, T., and Wieghardt, K., Eds.; Wiley & Sons: Chicester, New York, Weinheim, Brisbane, Singapore, Toronto, 2001; Vol. 2, pp 1284−1300.
(8) Youn, H.-D.; Youn, H.; Lee, J.-W.; Yim, Y.-I.; Lee, J.-K.; Hah, Y. C.; Kang, S.-O. *Arch. Biochem. Biophys.* **1996**, *334*, 341−348.
(9) Youn, H.-D.; Kim, E.-J.; Roe, J.-H.; Hah, Y. C.; Kang, S.-O. *Biochem. J.* **1996**, *318*, 889−896.
(10) Kim, E.-J.; Kim, H.-P.; Hah, Y. C.; Roe, J.-H. *Eur. J. Biochem.* **1996**, *241*, 178−185.
(11) Palenik, B.; Brahamsha, B.; Larimer, F. W.; Land, M.; Hauser, L.; Chain, P.; Lamerdin, J.; Regala, W.; Allen, E. E.; McCarren, J.; Paulsen, I.; Dufresne, A.; Partensky, F.; Webb, E. A.; Waterbury, J. *Nature* **2003**, *424*, 1037−1042.
(12) Mulrooney, S. B.; Hausinger, R. P. *FEMS Microbiol. Rev.* **2003**, *27*, 239−261.
(13) Choudhury, S. B.; Lee, J.-W.; Davidson, G.; Yim, Y.-I.; Bose, K.; Sharma, M. L.; Kang, S.-O.; Cabelli, D. E.; Maroney, M. J. *Biochemistry* **1999**, *38*, 3744−3752.

10.1021/ja053665f CCC: $33.50

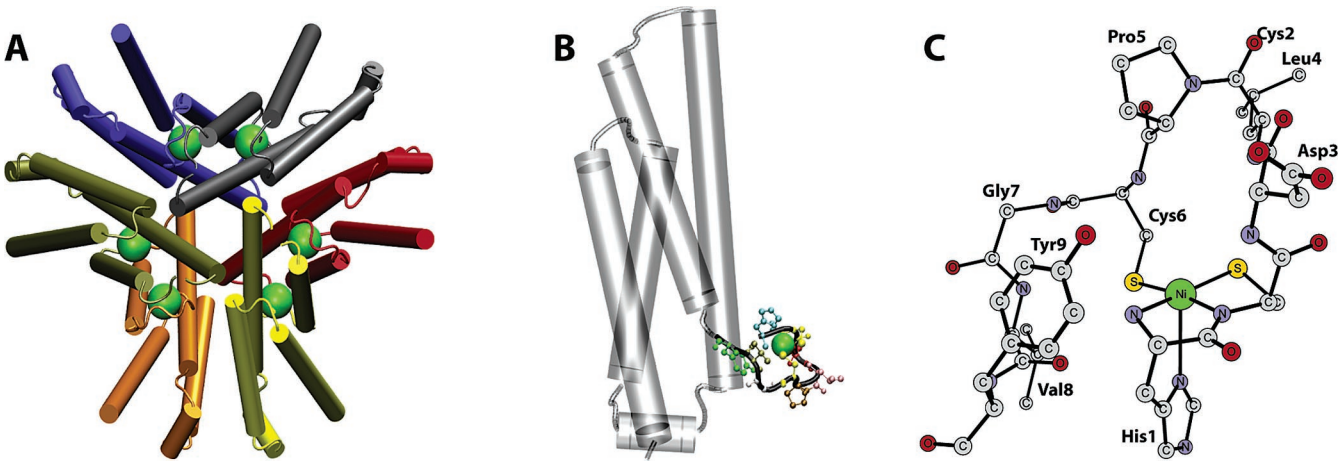

Figure 1. NiSOD 2.2 Å map resolution structure in the oxidized Ni(III) (resting) state as found in the 1Q0D[14] PDB file. Ni ions are given as green spheres. (A) The homohexamer overall structure. (B) The ribbon view of the monomer subunit, with the Ni-hook nine-residue structural motif shown in ball-and-stick representation. (C) The detailed view of the metal-chelating His-Cys-X-X-Pro-Cys-Gly-X-Tyr motif, forming the active site. Pictures A and B were generated using the VMD 1.8.2 molecular visualization program.[17]

determinations[14,15] reveal a homohexameric NiSOD, possessing a three-fold symmetry axis (Figure 1A). Composed of a four-helix bundle in the all-antiparallel topology, the monomer subunit is a quite small 117 amino acid protein (Figure 1B). The residues of the N-terminal loop form the metal-coordinating "Ni-hook" which is disordered in the absence of a bound metal ion.[14−16] Conserved between the known NiSODs, the Ni-hook His1-Cys2-X-X-Pro5-Cys6-Gly7-X-Tyr9 motif (Figure 1C) was proposed as a diagnostic[15] of this enzyme class. The nine-residue hook conformation in the hexamer is stabilized by the inter-subunit forces, further resulting in the restricted access to the Ni ion. The backbone nitrogen atoms of the Ni-hook residues His1, Asp3, Cys6, and Gly7 prevent the contact of the metal center with solvent, and the side chains of Pro5 and Tyr9 form the bottleneck of the active site chamber ~5 Å away from nickel.[14,15] The latter residues therefore impose size limits on NiSOD substrates and inhibitors. Close to the metal center, the active site channel terminus is as narrow as ~3 Å.[15]

The amine of N-terminal His1, the deprotonated backbone amide of Cys2, and the thiolates of Cys2 and Cys6 form a square planar framework of the Ni coordination sphere. This N2S2 ligand field with the metal incorporation into the backbone nitrogens and thiolate sulfurs is reminiscent of nickel coordination by the A-cluster of acetyl-coenzyme A (CoA) synthase (ACS).[18−20] Two distinct conformations for the His1 side chain were observed in the NiSOD active site: one with the axial Ni(III)−N^{δ}_{His1} coordination to the metal center in its oxidized (resting, or native) state (Figure 1C) or, alternatively, with the His1 imidazole ring tilted away from the metal (via the rotation around the $C_{\beta}-C_{\gamma}$ bond) in its reduced Ni(II) state. The resting square pyramidal Ni(III) can be reduced to a square planar Ni(II) chemically (with dithionite[13] or thiosulfate[14]) or under exposure to X-ray radiation.[14,15] As deduced from the hydrogen bonding network, His1 imidazole should be doubly protonated in the reduced state.[14] Based on these X-ray structures, and supported by analysis of EPR and XAS spectra,[9,13−15] NiSOD was proposed[15,21,22] to dismutate $O_2^{\bullet-}$ by analogy to the commonly accepted mechanism for CuZnSOD.[7,23,24] The Ni(III) reduction in this mechanism is redox-coupled to the protonation of His1, bound to the metal in its resting state (in CuZnSOD, this role is played by His61, bridging the oxidized Cu(II) and Zn(II)):

$$\mathrm{Ni(III)}-N^{\delta}_{His1} + O_2^{\bullet-} + H^+ \rightarrow \mathrm{Ni(II)} + H-N^{\delta+}_{His1} + O_2 \quad (2)$$

$$\mathrm{Ni(II)} + H-N^{\delta+}_{His1} + O_2^{\bullet-} + H^+ \rightarrow \mathrm{Ni(III)}-N^{\delta}_{His1} + H_2O_2 \quad (3)$$

The two successive superoxide radicals penetrate an ~7 Å deep active site channel and bind to the SOD active site in its two alternating states, producing a dioxygen molecule in the reductive phase, eq 2, and a hydrogen peroxide molecule in the oxidative phase, eq 3. $O_2^{\bullet-}$ contact with Ni can take place exclusively at the open axial coordination site opposite to the N^{δ}_{His1} metal ligand (above the metal center in Figure 1C). While formally similar to the catalysis by CuZnSOD, the two-step mechanism in eqs 2 and 3 is more complicated for NiSOD due to the topology of its active site. In contrast to N^{ϵ}_{His61} of CuZnSOD, N^{δ}_{His1} of NiSOD has no access to the active site chamber and is essentially blocked from the solvent. Even though the latter condition may vary when considering the enzyme dynamics or substrate binding, the presumed proton exchange at N^{δ}_{His1} of NiSOD is likely to be achieved only via a network of hydrogen-bonded proton mediators. Glu17 of the neighboring subunit has a contact to N^{ϵ}_{His1} via a hydrogen bond

(14) Wuerges, J.; Lee, J.-W.; Yim, Y.-I.; Yim, H.-S.; Kang, S.-O.; Carugo, K. D. *Proc. Natl. Acad. Sci. U.S.A.* **2004**, *101*, 8569−8574.
(15) Barondeau, D. P.; Kassmann, C. J.; Bruns, C. K.; Tainer, J. A.; Getzoff, E. D. *Biochemistry* **2004**, *43*, 8038−8047.
(16) Barondeau, D. P.; Getzoff, E. D. *Curr. Opin. Struct. Biol.* **2004**, *14*, 765−774.
(17) Humphrey, W.; Dalke, A.; Schulten, K. *J. Mol. Graphics* **1996**, *14*, 33−38.
(18) Doukov, T. I.; Iverson, T. M.; Seravalli, J.; Ragsdale, S. W.; Drennan, C. L. *Science* **2002**, *298*, 567−572.
(19) Darnault, C.; Volbeda, A.; Kim, E. J.; Legrand, P.; Vernede, X.; Lindahl, P. A.; C., F.-C. J. *Nat. Struct. Biol.* **2003**, *10*, 271−279.
(20) Svetlitchnyi, V.; Dobbek, H.; W., M.-K.; Meins, T.; Thiele, B.; Romer, P.; Huber, R.; Meyer, O. *Proc. Natl. Acad. Sci. U.S.A.* **2004**, *101*, 446−451.
(21) Bryngelson, P. A.; Arobo, S. E.; Pinkham, J. L.; Cabelli, D. E.; Maroney, M. J. *J. Am. Chem. Soc.* **2004**, *126*, 460−461.
(22) Miller, A.-F. *Curr. Opin. Chem. Biol.* **2004**, *8*, 162−168.
(23) Tainer, J. A.; Getzoff, E. D.; Richardson, J. S.; Richardson, D. C. *Nature* **1983**, *306*, 284−287.
(24) Hart, P. J.; Balbirnie, M. M.; Ogihara, N. L.; Nersissian, A. M.; Weiss, M. S.; Valentine, J. S.; Eisenberg, D. *Biochemistry* **1999**, *38*, 2167−2178.

in both the reduced and oxidized states. Arg47 from the same subunit as Glu17 is also in a nearby position. The Glu17 and Arg47 side chains therefore can communicate a proton between the interior solvent-accessible regions, observed for the NiSOD homohexamer,[14] and His1.

Similar to the suggestion made for [NiFe]hydrogenases,[25−27] the metal-bound Cys2 (or Cys6) thiolate of NiSOD could take part in the proton-coupled electron transfer[13,22,28] alternatively to the His1 imidazole in eqs 2 and 3:

$$\mathrm{Ni(III)}-\mathrm{S^-_{Cys2}} + \mathrm{O_2^{\bullet -}} + \mathrm{H^+} \rightarrow \mathrm{Ni(II)}-[\mathrm{H}-\mathrm{S_{Cys2}}] + \mathrm{O_2} \quad (4)$$

$$\mathrm{Ni(II)}-[\mathrm{H}-\mathrm{S_{Cys2}}] + \mathrm{O_2^{\bullet -}} + \mathrm{H^+} \rightarrow \mathrm{Ni(III)}-\mathrm{S^-_{Cys2}} + \mathrm{H_2O_2} \quad (5)$$

For the proton delivery from the solvent-accessible face of the Ni-coordinating N2S2 square plane, this mechanism implies less steric hindrance compared to the mechanism involving His1 protonation in eqs 2 and 3. His1 is however an essential residue for the enzyme activity according to mutagenesis studies.[14,21] In the mechanism described by eqs 4 and 5, the $\mathrm{N^{\delta}_{His1}}$ axial ligand therefore could distinctly modulate the metal properties during catalysis, as confirmed by the recent spectroscopic and computational study of NiSOD.[29]

An alternative scenario might involve a hybrid between the former two mechanisms. The metal-bound thiolate could serve as a transient proton location, shuttling the proton between the two faces of the N2S2 plane in the reduced state:

$$\mathrm{N^{\delta}_{His1}}-\mathrm{Ni(II)}-[\mathrm{H}-\mathrm{S_{Cys2}}] \rightleftharpoons \mathrm{N^{\delta +}_{His1}}-\mathrm{H} + \mathrm{Ni(II)}-\mathrm{S^-_{Cys2}} \quad (6)$$

Another widely debated aspect of SOD catalysis relates to inner-sphere versus outer-sphere mechanisms of electron transfer between the substrate and the metal ion. For NiSOD, the data collected on this subject are controversial. Electrostatic guidance of anionic superoxide consistent with the inner-sphere mechanism has been implicated in $\mathrm{O_2^{\bullet -}}$ scavenging by CuZnSOD;[7] however, its importance for NiSOD is debated.[13−15] A lack of strong dependence of the catalytic rate on ionic strength disfavors the importance of the electrostatic steering.[13] While the enzyme's activity is inhibited to 50% by 42 mM azide[13] and completely abolished by 10 mM cyanide,[9] interpretations of EPR spectra argue against binding of these inhibitor molecules to the nickel ion.[15] Calculation of the NiSOD solvent-accessible area predicts Ni and the N2S2 square plane atoms to be essentially buried. Still, a water molecule with elevated mobility is found close to the vacant axial position at ∼3.5 Å from Ni (with exclusion to the thiosulfate-reduced X-ray structure, where this distance is ∼4 Å).[14]

For an SOD enzyme to be active, the catalytic metal redox potential should be low enough to lie between the reduction potentials of $\mathrm{O_2}$ and $\mathrm{O_2^{\bullet -}}$.[30−32] In the absence of experimental data on the NiSOD redox potential, $E^{\circ\prime}$(Ni(III/II)) in aqueous solution or with O/N ligands is ∼1 V, while $E^{\circ\prime}(\mathrm{O_2/O_2^{\bullet -}}) = -0.16$ V and $E^{\circ\prime}(\mathrm{O_2^{\bullet -}/H_2O_2}) = +0.89$ V ($E^{\circ\prime}$ values are given vs the standard hydrogen electrode at 1 M, 25 °C and pH ≈ 7). However $E^{\circ\prime}$(Ni(III/II)) could be lowered using thiolate ligands, and Ni−cysteinate ligation is considered as a hallmark of redox-active nickel enzymes.[13,33]

The goal of the present study is to discriminate between the mechanistic proposals given above and thereby elucidate the catalytic pathway for NiSOD. The actual proton delivery to the reaction center and identity of the protonation site are of particular interest. The role of His1 in the catalytic process is also examined.

II. Computational Details

Most of the calculations were done using the B3LYP[34−36] hybrid density functional. Open-shell molecular systems were treated using unrestricted DFT. Geometry optimizations were generally performed using a standard valence LACVP basis set as implemented in the Jaguar 5.5 program.[37] For the first- and second-row elements, LACVP implies a 6-31G double-ζ basis set. For the nickel atom, LACVP uses a nonrelativistic effective core potential (ECP),[38] where the valence part is essentially of double-ζ quality. In an attempt to assess the quality of the Ni-ligand coordination geometry, additional calculations were done using the PW91[39] pure (nonhybrid) density functional and the LACVP* basis set, with the * option placing polarization functions on all atoms except H and Ni here. Local minima were optimized using the Jaguar 5.5 program. Analytical Hessians (second derivatives of the energy with respect to the nuclear coordinates) and the corresponding transition states were obtained using the Gaussian 98 program.[40] Accurate single-point energies ($E_{\mathrm{LACV3P^{**}}}$) were obtained using the LACV3P** basis set of triple-ζ quality, which has a larger valence basis set for nickel. For the rest of the atoms, LACV3P** implies a 6-311G** basis set with a single set of polarization functions added on all atoms except for transition metals. Contributions from solvent effects (E_{SOLV}) to the accurate energies were computed using the LACV3P** basis set for the gas-phase optimized geometries using a Poisson−Boltzmann solver[41,42] as implemented in Jaguar 5.5. The radius of the solvent probe molecule was set to 1.40 Å, corresponding to the water molecule. The dielectric constant ϵ of the protein was set to 4, in line with previous studies.[43] The Mulliken spin populations reported below in the text and figures are based on self-consistent reaction field (SCRF) spin densities, calculated using the LACV3P** basis set and including corrections from induced solvent charges. Thermochemical contributions[44] to the energies come from the internal thermal energy E_{THERM}

(25) Pavlov, M.; Siegbahn, P. E. M.; Blomberg, M. R. A.; Crabtree, R. H. *J. Am. Chem. Soc.* **1998**, *120*, 548−555.
(26) Niu, S.; Thomson, L. M.; Hall, M. B. *J. Am. Chem. Soc.* **1999**, *121*, 4000−4007.
(27) Amara, P.; Volbeda, A.; Fontecillia-Camps, J. C.; Field, M. J. *J. Am. Chem. Soc.* **1999**, *121*, 4468−4477.
(28) Szilagyi, R. K.; Bryngelson, P. A.; Maroney, M. J.; Hedman, B.; Hodgson, K. O.; Solomon, E. I. *J. Am. Chem. Soc.* **2004**, *126*, 3018−3019.
(29) Fiedler, A. T.; Bryngelson, P. A.; Maroney, M. J.; Brunold, T. C. *J. Am. Chem. Soc.* **2005**, *127*, 5449−5462.
(30) Stein, J. P.; Fackler, J. P. J.; McClune, G. J.; Fee, J. A.; Chan, L. T. *Inorg. Chem.* **1979**, *18*, 3511−3519.
(31) Barrette, W. C. J.; Sawyer, D. T.; Fee, J. A.; Asada, K. *Biochemistry* **1983**, *22*, 624−627.
(32) Noodleman, L.; Lovell, T.; Han, W.-G.; Li, J.; Himo, F. *Chem. Rev.* **2004**, *104*, 459−508.
(33) Maroney, M. J. *Curr. Opin. Chem. Biol.* **1999**, *3*, 188−199.
(34) Becke, A. D. *Phys. Rev. A* **1988**, *38*, 3098−3100.
(35) Becke, A. D. *J. Chem. Phys.* **1993**, *98*, 1372.
(36) Becke, A. D. *J. Chem. Phys.* **1993**, *98*, 5648.
(37) *Jaguar 5.5*; Schrödinger, L.L.C.: Portland, OR, 2003.
(38) Hay, P.; Wadt, W. *J. Chem. Phys.* **1985**, *82*, 299−310.
(39) Perdew, J. P.; Chevary, J. A.; Vosko, S. H.; Jackson, K. A.; Pederson, M. R.; Singh, D. J.; Fiolhais, C. *Phys. Rev. B* **1992**, *46*, 6671−6687.
(40) Frisch, M. J. et al. *Gaussian 98*; Gaussian Inc.: Pittsburgh, PA, 1998.
(41) Tannor, D.; Marten, B.; Murphy, R.; Friesner, R.; Sitkoff, D.; Nicholls, A.; Honig, B.; Ringnalda, M.; Goddard, W., III *J. Am. Chem. Soc.* **1994**, *116*, 11875−11882.
(42) Marten, B.; Kim, K.; Cortis, C.; Friesner, R.; Murphy, R.; Ringnalda, M.; Sitkoff, D.; Honig, B. *J. Phys. Chem.* **1996**, *100*, 11775−11788.
(43) Konecny, R.; Li, J.; Fisher, C. L.; Dillet, V.; Bashford, D.; Noodleman, L. *Inorg. Chem.* **1999**, *38*, 940−950.
(44) McQuarrie, D.; Simon, J. *Molecular Thermodynamics*; University Science Books: Sausalito, CA, 1999.

(including the zero-point energy) and entropy $-TS$, which were obtained for the optimized structures at the standard temperature $T = 298.15$ K, based on the computed Hessians. The ultimate Gibbs free energies include the individual terms described above:

$$G = E_{\mathrm{LACV3P**}} + E_{\mathrm{SOLV}} + E_{\mathrm{THERM}} - TS \tag{7}$$

The individual contributions for particular states are listed in Table 2. Note that in Table 2 the singlet/triplet state nomenclature implies the total spin of the active site plus reactant superoxide or product molecular oxygen, when applicable. Errors in the relative energies calculated using the scheme described above are usually within 3 kcal/mol and rarely exceed 5 kcal/mol.[45]

Open-shell calculations for the singlet ($S = 0$) states of biradical character (**2**^{1}, **3**^{1}, their prime and double-prime versions, and corresponding transition states **TS1**^{1}, **TS3**^{1}; see section III.b and Figure 2) resulted in a significant degree of spin contamination with $\langle S^2\rangle_{\mathbf{S}} = 1.1-1.5$ (= 0 for a pure singlet; **S** subscript stands for singlet); see Table 2. The high-spin triplet ($S = 1$) configurations of these states (**2**^{3}, **3**^{3}, **TS1**^{3}, **TS3**^{3}) resulted in $\langle S^2\rangle_{\mathbf{T}} = 2.1-2.2$ (= 2 for a pure triplet; **T** subscript stands for triplet). For the **4**^{1} singlet, the unrestricted calculation converged to a closed shell wave function, and no spin contamination was observed for the **4**^{3} triplet. For the doublet ($S = {}^1/_2$) states (**1**, **5**, **6**, **TS2**, **TS5**), the spin contamination is comparable to the triplet states with $\langle S^2\rangle_{\mathbf{D}} = 0.9-1.1$ (= 0.75 for a pure doublet). In the context of the present study, the most problematic issue of spin contamination is the inaccuracy of the singlet−triplet energy gap $\Delta_{\mathrm{unr,ST}}$ from unrestricted calculations. $\langle S^2\rangle$ values reported above imply that the singlet biradicals in particular suffer from admixtures of higher spin states (triplet, quintet, etc). A simple *spin projection* technique[46] postulating the triplet to be a pure spin state and the singlet to be contaminated only by the triplet component allows an estimation of the singlet−triplet gap for pure states. It can be shown[47] that the same result is obtained from the *broken symmetry* (BS) approach:[48]

$$\Delta_{\mathbf{ST}}^{\mathrm{BS}} = \frac{2}{2 - \langle S^2\rangle_{\mathbf{S}}}\Delta_{\mathrm{unr,ST}} \tag{8}$$

The high-spin biradicals obtained here are however not pure triplet states either; assuming that the contributions from all the higher spin states (quintet, septet, etc) for both the singlet and triplet are equal, a corrected expression which accounts for $\langle S^2\rangle_{\mathbf{T}}$ would be

$$\Delta_{\mathbf{ST}} = \frac{2}{\langle S^2\rangle_{\mathbf{T}} - \langle S^2\rangle_{\mathbf{S}}}\Delta_{\mathrm{unr,ST}} \tag{9}$$

The formula in eq 8 is a special case of the formula in eq 9 for a pure triplet with $\langle S^2\rangle_{\mathbf{T}} = 2$. It is therefore clear that

$$\Delta_{\mathrm{unr,ST}} < \Delta_{\mathbf{ST}} < \Delta_{\mathbf{ST}}^{\mathrm{BS}} \tag{10}$$

The low-spin $E_{\mathrm{LACV3P**}}$ energies for the biradical states were corrected using eq 9. This affects only the singlet surface of the reductive half-reaction; see below. The singlet−triplet gap correction

$$\delta_{\mathbf{ST}} = \Delta_{\mathbf{ST}} - \Delta_{\mathrm{unr,ST}} \tag{11}$$

is normally small (see Table 1) and reaches its maximum absolute value of 5.9 kcal/mol for state **3**.

A separate comment should be given on the estimation of the entropy contributions to the relative energies along the potential energy surface. The gas-phase calculations for the substrate and products of the dismutation would overestimate the absolute entropy values. Precisely prior to binding and after release, the molecular species are confined within the narrow active site channel and can move freely only a very short distance. The translational entropy S_{tr} contribution to the molar entropy in this case can be approximated using the modified Sackur−Tetrode equation:[49]

$$S_{\mathrm{tr}} = R\left(\ln\frac{\upsilon_{\mathrm{f}}}{\Lambda^3} + \frac{5}{2}\right) \tag{12}$$

where R is the gas constant, Λ is the thermal de Broglie wavelength of a molecule, and υ_{f} is the free volume in which the center of mass of a molecule can move inside the cavity. For NiSOD, the diameter of the active site chamber at its base is ∼3.0 Å; see section I. Taking into account the size of a reactant or product molecule, a simple estimate for the free volume would be a spherical cavity of 1.0 Å radius with impenetrable walls. For the superoxide radical, hydrogen peroxide, and dioxygen this leads to a TS_{tr} value of 5.4 kcal/mol, as compared to the calculated gas-phase 10.8−10.9 kcal/mol range. Rotational S_{rot} and vibrational S_{vibr} entropies contribute less significantly to the total entropy, as compared to S_{tr}. S_{rot} and S_{vibr} estimates for a molecule in a cavity are not straightforward, and calculated gas-phase values were used here.

When discussing the free energy change ΔG_{OOH} required for the protonation of the $O_2^{\bullet-}$ superoxide radical anion in solution, the following evaluation was used:

$$\begin{aligned}\Delta G_{\mathrm{OOH}} &= -RT\ln\frac{[^{\bullet}\mathrm{OOH}]}{[\mathrm{O_2^{\bullet-}}]} = RT\left(\ln\frac{[\mathrm{H^+}][\mathrm{O_2^{\bullet-}}]}{[^{\bullet}\mathrm{OOH}]} - \ln[\mathrm{H^+}]\right)\\ &= RT\ln 10\left(\log_{10}\frac{[\mathrm{H^+}][\mathrm{O_2^{\bullet-}}]}{[^{\bullet}\mathrm{OOH}]} - \log_{10}[\mathrm{H^+}]\right)\\ &= RT\ln 10(\mathrm{pH} - \mathrm{p}K_{\mathrm{a}}(\mathrm{OOH}))\\ &= 1.36(7 - 4.8)\ \mathrm{kcal/mol} = 3.0\ \mathrm{kcal/mol}\end{aligned} \tag{13}$$

where the experimental $\mathrm{p}K_{\mathrm{a}}(\mathrm{OOH}) = 4.8$ for the hydroperoxyl (hydrogen dioxide, hydrodioxyl, or perhydroxyl) $^{\bullet}$OOH radical[50] was used.

The free energy change associated with the electron-transfer reactions is calculated from the Nernst equation:

$$\Delta G^{\circ\prime} = -nF\Delta E^{\circ\prime} \tag{14}$$

where n is the number of electrons exchanged in the process, $F = 23.06$ kcal/mol V is the Faraday constant, and $\Delta E^{\circ\prime}$ is the corresponding electromotive force.

Table 1. Singlet−Triplet Splittings, kcal/mol, for the States of Biradical Character: $\Delta_{\mathrm{unr,ST}}$ from the Unrestricted Calculations; $\Delta_{\mathrm{ST}}^{\mathrm{BS}}$ from the Broken Symmetry (or Spin Projection) Approach; (See eq 8); the Presently Proposed Δ_{ST} (See eq 9) and the Final Singlet-Triplet Gap Correction δ_{ST} (See eq 11)

state[a]	$\Delta_{\mathrm{unr,ST}}$	$\Delta_{\mathrm{ST}}^{\mathrm{BS}}$	Δ_{ST}	δ_{ST}
2	0.6	1.5	1.2	0.6
2′′	0.5	1.1	1.0	0.5
TS1	0.8	2.0	1.6	0.8
3	−3.2	−12.8	−9.1	−5.9
3′′	2.0	8.0	6.7	4.7
TS3	2.6	6.5	5.2	2.6
3′	0.7	1.6	1.4	0.7

[a] The classification of the states is given in section III.b.

(45) Siegbahn, P. *Q. Rev. Biophys.* **2003**, *36*, 91−145.
(46) Ovchinnikov, A. A.; Labanowski, J. K. *Phys. Rev. A* **1996**, *53*, 3946−3952.
(47) Ciofini, I.; Daul, C. A. *Coord. Chem. Rev.* **2003**, *238*−*239*, 187−209.
(48) Noodleman, L. *J. Chem. Phys.* **1981**, *74*, 5737−5743.
(49) Amzel, L. M. *Proteins* **1997**, *28*, 144−149.
(50) Bielski, B. H. J.; Cabelli, D. E.; Arudi, R. L.; Ross, A. B. *J. Phys. Chem. Ref. Data* **1985**, *14*, 1041−1100.

III. Results and Discussion

III.a. Chemical Models. The Ni-hook His1-Cys2-X-X-Pro5-Cys6-Gly7-X-Tyr9 motif is characteristic for NiSOD and represents a very compact incorporation of the active site by the backbone. Despite the proposed importance of the intersubunit interactions (see section **I**) for the active site conformation, a model for a mechanistic study can be limited by the Ni-hook residues. However, inclusion of every side chain member in this nine-residue sequence spacer does not appear necessary. Pro5 plays a hinge role, and Tyr9 provides a gating function for the enzyme selectivity. Asp3, Leu4, and Val8 probably play only secondary roles during catalysis. Only His1, Cys2, and Cys6 are likely to be of principal importance during the actual dismutation of superoxides, as well as for the metal coordination. Therefore only these three Ni-hook residues were modeled together with their side chains. The polypeptide backbone connecting these residues was also included in the model, with the rest of the side chains omitted and the α-carbons saturated by hydrogens at the β-carbon positions. Retaining the linking backbone gives a structural stability of the model and also leads to a realistic positioning of the chemical units, which is otherwise often achieved only via artificial fixations of specific nuclear coordinates.[51,52] Crystal structures found in the 1Q0D and 1Q0M PDB files[14] were used for the modeling of the oxidized and reduced states.

Before the substrate arrival, the cluster described above together with the Ni center in its core contains 58 atoms. This is an average system size for B3LYP calculations,[45] and its possible extension is an attractive target for a QM/MM modeling. A possible setup can be done similarly to what was done previously in an ONIOM(B3LYP:MNDO) study on the hydrolysis by MMP,[53] which used the active site formed by the His-Glu-X-X-His-X-X-Gly-X-X-His backbone spacer, coordinating Zn(II). The present system is of zero charge. The spin state for the native resting Ni(III) enzyme is a doublet.

III.b. Dismutation Mechanism. The source of two protons required for the dismutation reaction, eq 1, and the associated energetics is very important for the NiSOD catalysis. Among several candidates, the backbone amides of Asp3 or Cys6 and the side chain phenol of Tyr9 were considered as potential proton donors for the superoxide, while it accesses the Ni center moving through the pocket.[14,15] Due to the steric hindrance as discussed in section **I**, His1 in its protonated form is a less likely proton donor during the oxidative phase. However, the primary source of the protons is the surrounding bulk water. An immediate proton donor to superoxide could be a group within the active site which is reprotonated later from the solvent. The protons then can be considered implicitly as a combined delivery of $O_2^{\bullet-}$ and H^+, similarly to what was done in a recent study of catalysis by CuZnSOD.[54] The energy cost to protonate $O_2^{\bullet-}$ at pH = 7 is 3.0 kcal/mol, as estimated in section II. The resulting $^{\bullet}$OOH hydroperoxyl radical is then postulated to be the immediate substrate for SOD, bearing in mind the 3.0 kcal/mol correction when discussing the relative energies along the reaction path. The correction to the translational entropy of the inbound substrate and products (see section II) is also included below.

The tightly linked approach of $O_2^{\bullet-}$ and H^+ to the active site implies a unified scheme of proton delivery in both the reductive and oxidative phases here. Ideally, the proton delivered during the reductive phase to the resting Ni(III) enzyme should be located in the vicinity of Ni(II) before the oxidative phase starts. This will probably retain the debated electrostatic steering factor (see section I) which is similar for the two successive substrate molecules. In view of the arguments in section I, the thiolate sulfur of Cys2 or Cys6 can be a direct proton acceptor from the inbound protonated superoxide during the reductive phase, eq 4. After the O_2 product release, this thiolate could host the proton and donate it to the second incoming protonated superoxide molecule during the oxidative phase, eq 5, forming H_2O_2. Examination of the active site structure suggests that S^-_{Cys2} has a larger electronic density at the solvent-accessible face of the N2S2 plane, as compared to S^-_{Cys6}, and therefore would be a preferred H^+ acceptor (implying sp^3 hybridized orbitals, for S^-_{Cys2} the two lone pairs should be directed at the different faces of the N2S2 plane; for S^-_{Cys6} both the lone pairs should be directed toward the solvent-inaccessible face).

Reductive Phase and O_2 Formation. Ferromagnetic (S = 1) and antiferromagentic (S = 0) couplings of the $^{\bullet}$OOH hydroperoxyl radical and the doublet ($S = {}^1/_2$) Ni(III) d^7 resting state **1** (see Figure 2) lead to two spin surfaces for the reductive half-reaction. For the Ni(III) states **2**−**3**, the singlet and triplet spin states have biradical character and are not degenerate, as reflected in Figure 5 and Table 2. For the square pyramidal Ni(II) d^8 state **4**, arising after the triplet O_2 release, a singlet−triplet $\mathbf{4}^1$−$\mathbf{4}^3$ gap of 10.0 kcal/mol was found favoring the triplet metal state ($\mathbf{4}^3 + \mathbf{O}_2$ is −7.0 kcal/mol, and $\mathbf{4}^1 + \mathbf{O}_2$ is 3.0 kcal/mol). Taking into account the O_2 molecule release, this implies that a spin crossover is necessary in case the reaction starts at the overall triplet surface, as shown in Figure 5.

The nonreductive binding of the substrate to Ni(III) in **2** is favorable (by 11.4−12.6 kcal/mol; see $E_{LACV3P**}$ in Table 2) only when the entropy and solvent effect contributions to the free energy are omitted. Similarly, state **3** with the metal-bound superoxide is only metastable. States **2** and **3** are intermediates only at the LACVP geometry optimization level. The **TS1** transition state (see Figure 3 for the singlet $\mathbf{TS1}^1$ structure) involves a proton transfer between the *distal* oxygen of the bound hydroperoxyl and S^-_{Cys2} and links states **2** and **3**. Notably, the diffuse orbitals of S^-_{Cys2} allow the sulfur to nickel coordination to be retained at the transition state (S^-_{Cys2}−Ni(III) = 2.41 Å). The activation energies for **TS1** is 9.7 and 7.6 kcal/mol at the singlet ($\mathbf{TS1}^1$) and triplet ($\mathbf{TS1}^3$) spin surfaces, respectively. The final step $\mathbf{3} \rightarrow \mathbf{4} + \mathbf{O}_2$ of the half-reaction involves Ni reduction coupled to O_2 release, largely driven by the entropy factor. This occurs without any activation barrier. The reductive half-reaction is exergonic by 7.0 kcal/mol and terminated at $\mathbf{4}^3$.

Oxidative Phase and H_2O_2 Formation. The oxidative phase proceeds on the doublet spin surface. The $^{\bullet}$OOH substrate molecule antiferromagnetically couples to the high spin (S = 1) Ni(II) d^8 state $\mathbf{4}^3$. The oxidative binding results in an $^-$OOH hydroperoxide anion axially bound to the doublet Ni(III) d^7 in

(51) Pelmenschikov, V.; Siegbahn, P. E. M. *J. Biol. Inorg. Chem.* **2003**, *8*, 653−662.
(52) Pelmenschikov, V.; Cho, K.-B.; Siegbahn, P. E. M. *J. Comput. Chem.* **2004**, *25*, 311−321.
(53) Pelmenschikov, V.; Siegbahn, P. E. M. *Inorg. Chem.* **2002**, *41*, 5659−5666.
(54) Pelmenschikov, V.; Siegbahn, P. E. M. *Inorg. Chem.* **2005**, *44*, 3311−3320.

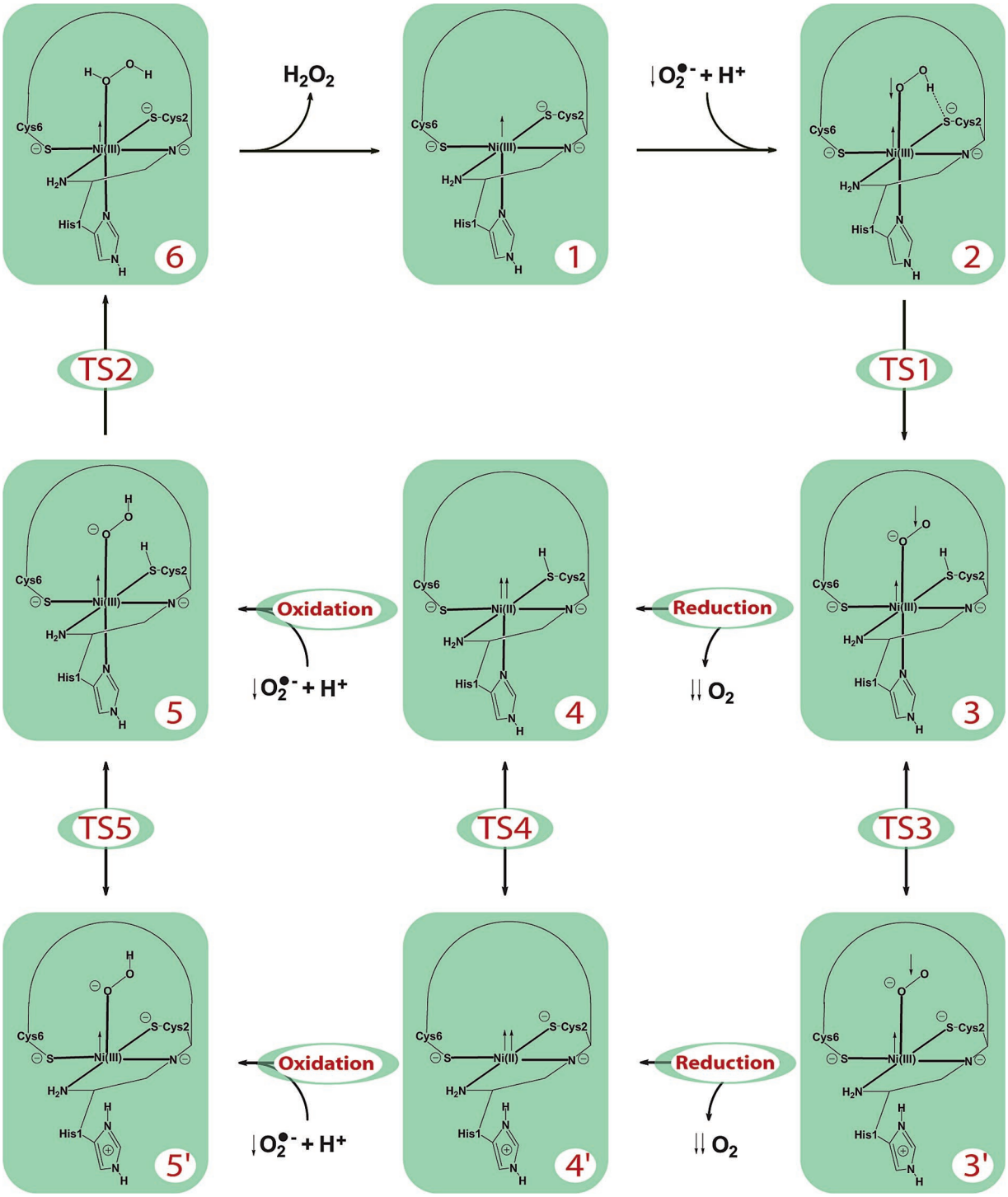

Figure 2. Chart showing the presently investigated states of NiSOD (double-prime states **1″**−**6″** are not shown here; see the text). See the Supporting Information for the corresponding coordinates. The upper cycle spanning nonprime states **1**−**6** represents the currently proposed reaction mechanism, with the two transition states **TS1** and **TS2** (see Figure 3 and Figure 4 for the structures). The prime states **3′**−**5′** lie outside the normal reaction pathway. For the reductive phase, the overall singlet spin states are shown.

state $\mathbf{5}^2$. In the case of ferromagnetic coupling, this would require the formation of a quartet ($S = {}^3/_2$) Ni(III) which is unprecedented in biochemistry. The redox binding process is strongly exothermic in gas phase with 25.2 kcal/mol at the LACV3P** level, but the entropy and E_{SOLV} contributions balance this $\mathbf{4}^3 + O_2^{\bullet-} \rightarrow \mathbf{5}^2$ step. The H_2O_2 product is formed at the **TS2** transition state (see Figure 4) involving the proton transfer between the H−S_{Cys2} and the *proximal* oxygen of the metal-bound hydroxide. The interligand proton transfer in the cyclic **TS2** imposes a considerable degree of strain and forces the sulfur to nickel coordination to become nearly lost (S^-_{Cys2}−Ni(III) = 2.68 Å). The activation energy for **TS2** is 12.1 kcal/mol (starting from the **5** state), and this is the rate-limiting process of the dismutation reaction (Figure 5). The H_2O_2 to Ni(III) binding LACV3P** energy in **6** is 12.2 kcal/mol, which is similar to the $^{\bullet}$OOH binding in **2**. This binding is turned into repulsion

Table 2. $\langle S^2 \rangle$ Values for the Metal-Containing Cluster, Mulliken ρ(Ni) Spin Density at Ni and Contributions to the Energies (kcal/mol) of the Reductive and Oxidative Half-Reactions, Relative to the Reactants **1** + $O_2^{\bullet-}$ and **4** + $O_2^{\bullet-}$ (see also Figure 5)[a]

state[b]	$\langle S^2 \rangle$	ρ(Ni)	$E_{LACV3P**}$[c]	E_{SOLV}	E_{THERM}	$-TS$	$\Delta_{tr}(-TS)$[d]	ΔG_{OOH}[e]	G
1 + $O_2^{\bullet-}$	0.9	1.12	0.0	0.0	0.0	0.0	0.0	0.0	0.0
1″ + $O_2^{\bullet-}$	0.8	0.84	2.4	3.9	−	−	0.0	0.0	6.3
2	1.2/2.2	1.17/1.10	−11.4/−12.6	7.2/7.3	0.2/1.1	15.6/12.2	−5.5	3.0	9.2/5.5
2″	1.1/2.1	1.12/1.03	−2.1/−3.1	9.2/8.9	−	−	−5.5	3.0	20.4/18.6
TS1	1.2/2.2	1.15/1.09	−8.9/−10.5	7.4/7.4	−1.5/−1.5	15.1/14.6	−5.5	3.0	9.7/7.6
3	1.5/2.2	1.37/1.12	−22.3/−13.2	7.6/6.5	0.2/0.1	13.5/13.1	−5.5	3.0	−3.5/4.3
3″	1.5/2.1	1.38/0.80	−1.0/−7.7	11.4/10.1	−	−	−5.5	3.0	21.6/13.6
TS3	1.2/2.2	1.13/1.04	12.1/6.9	2.6/2.7	−	−	−5.5	3.0	25.9/20.8
3′	1.1/2.1	1.04/0.88	−6.3/−7.7	1.2/−0.1	2.2/2.9	14.1/12.3	−5.5	3.0	8.7/4.9
4[f] + O_2	2.0/0.0	1.61/0.00	−19.8/−11.7	10.0/11.1	−1.1/−1.0	0.9/1.7	−0.03	3.0	−7.0/3.0
4″[f] + O_2	2.0/0.0	1.53/0.00	−16.2/−19.6	12.1/11.7	−/−1.1	-/4.0	−0.03	3.0	1.6/−2.1
TS4[f] + O_2	2.0/0.0	1.57/0.00	0.6/1.6	4.7/6.3	−	−	−0.03	3.0	8.1/10.7
4′[f] + O_2	2.0/0.0	1.54/0.00	3.5/−7.6	−1.3/−0.2	−/−2.3	−/2.3	−0.03	3.0	5.2/−4.8
4[3] + $O_2^{\bullet-}$	2.0	1.61	0.0	0.0	0.0	0.0	0.0	0.0	0.0
5	1.1	1.21	−25.2	7.5	2.9	16.8	−5.5	3.0	−0.6
5″	0.9	1.09	−12.7	3.1	−	−	−5.5	3.0	7.5
TS5	0.9	1.05	−1.1	3.4	−	−	−5.5	3.0	18.2
5′	0.9	1.11	−9.6	−5.9	4.7	13.5	−5.5	3.0	0.2
TS2	1.1	1.27	−12.3	8.5	0.9	16.9	−5.5	3.0	11.5
6	0.9	1.17	−27.4	7.2	4.7	15.4	−5.5	3.0	−2.6
6″	0.9	1.13	−21.4	8.0	−	−	−5.5	3.0	4.2
1 + H_2O_2	0.9	1.12	−15.2	−7.2	2.2	0.2	0.02	3.0	−17.0

[a] For the reductive phase, singlet and triplet spin state energies are given with a slash separator (singlet/triplet). In cases when the data on thermochemical corrections are missing, the total G free energies are estimated based on E_{THERM} and $-TS$ contributions for the corresponding nonprime states. [b] The classifications of the states is given in section III.b. [c] For the states of biradical character, the singlet state $E_{LACV3P**}$ unrestricted energies were corrected by δ_{ST}; see Table 1. [d] $\Delta_{tr}(-TS)$ implies correction to the translational contributions of the entropy according to eq 12. [e] ΔG_{OOH} is the correction due to the pH factor; see eq 13. [f] The overall singlet state here implies the Ni-containing cluster to be triplet and vice versa. For the singlet, unrestricted calculations resulted here in a closed shell wave function; for the triplet, a pure spin state was obtained.

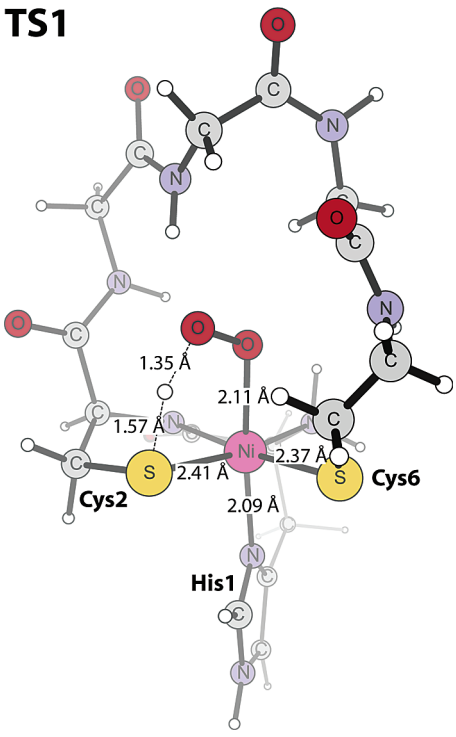

Figure 3. Transition state **TS1**[1] of the presently proposed mechanism, involving O_2 formation. Important distances are given. The corresponding imaginary frequency is −685 cm^{-1}; see the Supporting Information for the visulalized vibration.

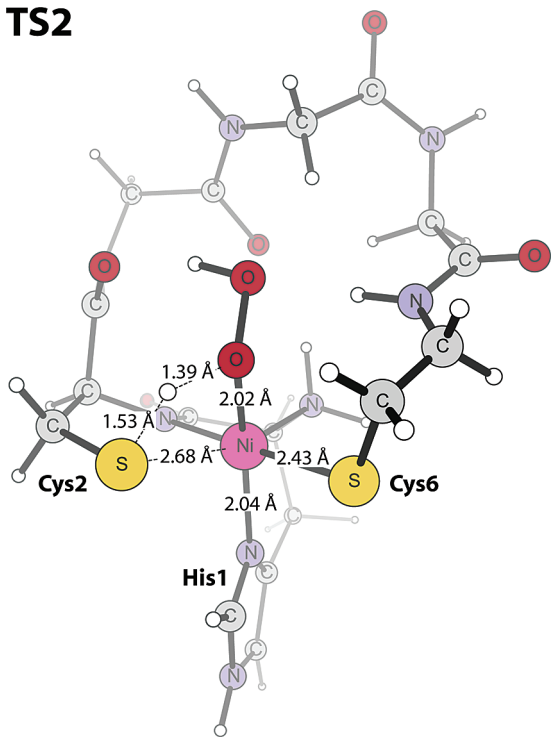

Figure 4. Transition state **TS2** of the presently proposed mechanism, involving H_2O_2 formation. Important distances are given. The corresponding imaginary frequency is −523 cm^{-1}; see the Supporting Information for the visulalized vibration.

by the entropy and E_{SOLV} factors. The oxidative half-reaction is exergonic by 17.0 kcal/mol.

III.c. Importance of His1. The His1 residue has been experimentally shown to be extremely important for the NiSOD catalytic function. The His1Gln mutation produces an enzyme with only ∼1% activity[21] of the wild-type NiSOD. A set of His1 mutants were recently reported[14] to give very small (<5%) enzyme activities. While a proton-donating role was previously attributed for His1 during the oxidative phase as in eq 3, in the present mechanism the Ni−N^{δ}_{His1} coordination remains intact

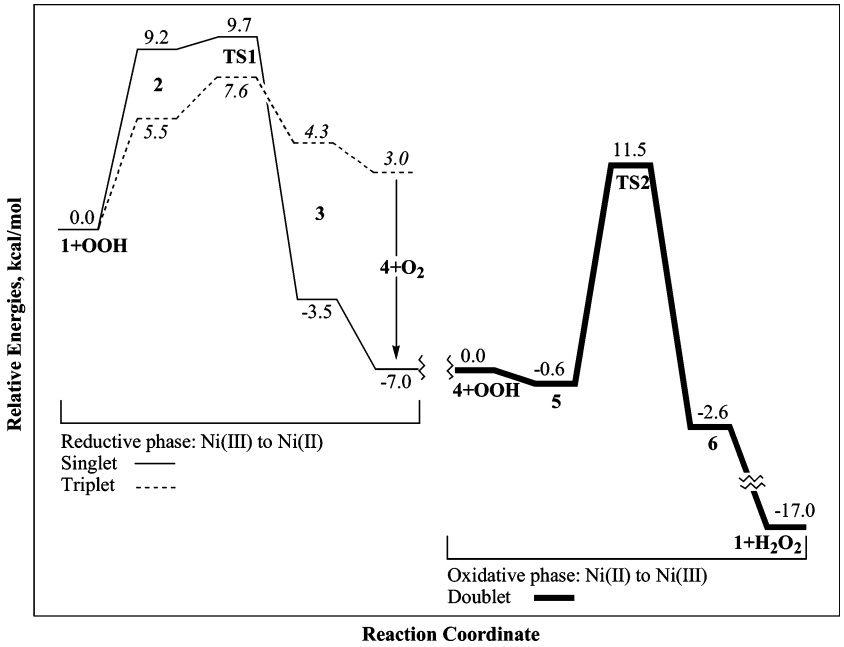

Figure 5. Free energy profile obtained for the two half-reactions catalyzed by NiSOD (involving nonprime states only). Individual contributions to the free energy values are given in Table 2. The vertical arrow symbolizes a spin transition for state **4**.

(states **1**−**6**, **TS1**, **TS2**, see Figure 2). For all the oxidized metal states, the Ni(III)−N^{δ}_{His1} axial coordination was found favorable with at least 6.3 kcal/mol (see Table 2) for the **1**″−**1** splitting (*double-prime states* imply that the Ni−His1 coordination was intentionally destroyed, and the structures were then reoptimized without any constraints). Maximal splittings of 25.1 and 13.1 kcal/mol at the singlet and triplet spin surfaces, respectively, were found for the $\mathbf{3''}^1-\mathbf{3}^1$ and $\mathbf{2''}^3-\mathbf{2}^3$ gaps. The relative energies of the double-prime states provide a possible explanation for the lack of activity of the His1-deficient enzyme. Indeed, relative to **1**″ + $O_2^{\bullet-}$, state **2**″ is 14.1/12.3 kcal/mol (singlet/triplet) and state **3**″ is 15.3/7.3 kcal/mol higher. Therefore, the relative **2**″ vs **2** increase is 4.9/6.8 kcal/mol, and the **3**″ vs **3** increase is 18.8/3.0 kcal/mol. This implies that the **1**″ + $O_2^{\bullet-}$ → **TS1**″ activation energy should be at least 3.0 kcal/mol higher than **1** + $O_2^{\bullet-}$ → **TS1**. Analysis of the energetics of the oxidative phase shows that the activation energy **5**″ → **TS2**″ for the double-prime surfaces should be essentially the same as that for **5** → **TS2** (the **5**″−**5** splitting is 8.1 kcal/mol, and the **6**″−**6** splitting is 6.8 kcal/mol). A depletion in activity of 2 orders of magnitude observed for the His1 mutants corresponds to a rate-limiting activation barrier increase by 3 kcal/mol only. It is very likely therefore that in the absence of the Ni(III)−N^{δ}_{His1} axial coordination, modeled by the double-prime states, the reductive phase activation barrier is the rate-limiting process and this is very slow compared to the native NiSOD kinetics.

A separate comment should be given on the Ni(II) square planar state **4**″, which shows a small $\mathbf{4''}^3-\mathbf{4''}^1$ splitting of 3.7 kcal/mol favoring the singlet. This is in contrast to the square pyramidal coordination of Ni(II) in **4**, favoring the triplet by 10.0 kcal/mol as discussed above. Among all the nonprime states, only for the low-spin reduced state **4** is the Ni(II)−N^{δ}_{His1} coordination unlikely, with a negative $\mathbf{4''}^1-\mathbf{4}^1$ gap of −5.1 kcal/mol. Preference toward a square planar coordination and axial ligand release is expected for the low-spin Ni(II).

Relocation of the H−S_{Cys2} proton to N^{δ} generates the experimentally observed diamagnetic square planar state $\mathbf{4'}^1$ (here and below, *prime states* imply no Ni−His1 coordination, and the proton located at N^{δ}_{His1} instead of S^{-}_{Cys2}; see Figure 2). $\mathbf{4'}^1$ is only 2.2 kcal/mol higher than the most stable reduced state $\mathbf{4}^3$ presently found. In view of the mechanism proposed here NiSOD can actually bypass the observed reduced state $\mathbf{4'}^1$ when disproportionating superoxides. See also the following subsection evolving this idea.

III.d. Proton Mediators, Alternative to S^{-}_{Cys2}. In the present mechanism it is suggested that in the interim between the two half-reactions the S^{-}_{Cys2} thiolate sulfur remains protonated (state **4**, Figure 2). The proton located at S^{-}_{Cys2} is necessary for the H_2O_2 formation during the oxidative phase. However, this proton can easily migrate, considering that O_2 product release to the outside and the subsequent substrate molecule approach are relatively slow diffusion processes. The proton migration can take place even before O_2 release (at **3**) and immediately after the $^{\bullet}$OOH coordination (at **5**). Therefore, alternative proton locations should be considered for states **3**, **4**, and **5**.

In view of the structural data and the mechanistic proposals in eqs 2 and 3, a likely candidate for an alternative proton location is His1. Within the constant proton content model, N^{δ}_{His1} can receive a proton from S^{-}_{Cys2} as suggested in eq 6. Among all the states with H−S_{Cys2} protonation, only the low-spin reduced Ni(II) $\mathbf{4}^1$ was found to easily lose the axial N^{δ}_{His1} ligand, resulting in $\mathbf{4''}^1$. The singlet $\mathbf{4''}^1$ can undergo proton transfer to $\mathbf{4'}^1$, which is favorable by 2.7 kcal/mol. However an obstacle for this conversion is the proton-transfer transition state $\mathbf{4''}^1$ → $\mathbf{TS4}^1$, which is 12.8 kcal/mol. Starting from the ground state $\mathbf{4}^3$ for the reduced metal cluster (square pyramidal high-spin Ni(II)), this $\mathbf{4}^3$→$\mathbf{TS4}^1$ transition state is 17.7 kcal/mol high. $\mathbf{4}^3$ → $\mathbf{TS4}^3$ has a somewhat lower activation energy of 15.1 kcal/mol. $\mathbf{TS4}^3$ will also imply a subsequent triplet-to-singlet conversion for **4**′, given that the $\mathbf{4'}^3-\mathbf{4'}^1$ gap is 10.0 kcal/mol.

For the Ni(III) states, the splittings between the nonprime and prime states are as follows: $\mathbf{3'}^1-\mathbf{3}^1$ is 12.2 kcal/mol, $\mathbf{3'}^3-\mathbf{3}^3$ is 0.6 kcal/mol, and $\mathbf{5'}^2-\mathbf{5}^2$ is 0.8 kcal/mol. Again, the direct proton-transfer activation barriers between the S^-_{Cys2} and N^{δ}_{His1} sites are high: $\mathbf{3}^1\rightarrow\mathbf{TS3}^1$ is 29.4 kcal/mol, $\mathbf{3}^3\rightarrow\mathbf{TS3}^3$ is 16.5 kcal/mol, and $\mathbf{5}^2\rightarrow\mathbf{TS5}^2$ is 18.8 kcal/mol.

The backbone amide of Cys6 was also tried as a proton mediator, alternative to S^-_{Cys2}. The proton migration to the backbone was not studied systematically, but only for state $\mathbf{3}^3$, leading to a state ~15 kcal/mol higher in energy relative to $\mathbf{3}^3$.

The results reported above imply that (*i*) based on the relative energies, the protonation of N^{δ}_{His1} vs S^-_{Cys2} cannot be ruled out; (*ii*) however, in the absence of additional proton donors to N^{δ}_{His1} besides $H-S_{Cys2}$ the direct proton transfer between these two locations is not likely. The **TS1** and **TS2** rate-limiting barriers of the reductive and oxidative half-reactions are smaller than **TS3**, **TS4**, and **TS5**, and therefore the prime states can be regarded as local minima lying outside the normal reaction pathway. Also, (*iii*) the backbone amides in the active site are disfavored as proton mediators.

III.e. On Possibility of the Reductive Phase Proceeding without an Extra Proton. One more alternative to the mechanism explored above is O_2 formation bypassing the involvement of a solvent proton. In this scenario, it is problematic to estimate the binding energy of the anionic $O_2^{\bullet-}$ to the active site. An enzyme−substrate complex $\mathbf{3}^-$ (with a proton missing at S_{Cys2} in contrast to **3**) with Ni(III)-bound superoxide will be considered here as an initial point. The triplet $\mathbf{3}^{-3}$ is the ground spin state with a singlet−triplet gap $\mathbf{3}^{-1}-\mathbf{3}^{-3}$ of 2.2 kcal/mol. Starting from $\mathbf{3}^{-3}$, the metal reduction concomitant with the O_2 release is exergonic by 8.3 kcal/mol, producing the Ni(II) state $\mathbf{4}^-$ (with a proton missing at S^-_{Cys2} in contrast to **4**). Similarly to the product release steps described above, this process is entropy-driven. The triplet and singlet surfaces are degenerate for $\mathbf{4}^-$, with the singlet−triplet gap $\mathbf{4}^{-1}-\mathbf{4}^{-3}$ less than 0.1 kcal/mol.

III.f. Ni-Ligand Bond Lengths. The present geometry optimization (B3LYP/LACVP) results in relatively long Ni−thiolate bonding distances of 2.33 ± 0.05 Å (averaged between the 21 Ni−thiolate $Ni-S^-_{Cys2}$ and $Ni-S^-_{Cys6}$ bond lengths for local minima in Table 3), as compared to the corresponding values from the NiSOD X-ray structure analysis: 2.16−2.19 Å by Wuerges et al.[14] and 2.18−2.30 Å by Barondeau et al.[15] (here and below, standard deviation errors are used). The overestimation of the Ni−thiolate bond lengths is also implied by the corresponding value of 2.24 ± 0.12 Å from the Cambridge Structural Database (CSD),[15,60] as averaged over more than 5400 samples. A modified geometry optimization approach has been examined, using (*i*) the PW91 functional and (*ii*) a larger LACVP* basis set. See the Supporting Information for the Ni−ligand bond lengths optimized using different methods. PW91/LACVP* predicts the Ni−thiolate bond lengths of 2.26 ± 0.04 Å, ~0.1 Å shorter as compared to those by B3LYP/LACVP and in better agreement with the above experimental data. The metal-to-protonated thiol distances were found sensitive to the modified optimization method as well, again becoming ~0.1 Å shorter: 2.33 ± 0.14 Å from PW91/LACVP* vs 2.43 ± 0.16 Å from B3LYP/LACVP (averaged between the 9 Ni−[H−S_{Cys2}] bond lengths in Table 3). For the Ni−thiol coordination, PW91 most probably underestimates the bond distances and B3LYP performs better, since the limited data (five examples from CSD) on Ni−thiol bond lengths are 2.46 ± 0.14 Å.[15] The present observation is that it is mainly the PW91 functional, not the basis set enlargement, that is responsible for the bond distance shift. Since the present study primarily concerns the energetics, the relative single-point B3LYP/LACV3P** energies (corresponding to $E_{LACV3P**}$ in Table 2) were compared for the 15 local minima in Table 3, optimized using B3LYP/LACVP and PW91/LACVP*. The average absolute deviation between the B3LYP/LACV3P** potential energy surfaces for the B3LYP/LACVP and PW91/LACVP* structures is 0.7 kcal/mol only, and the maximum deviation is 3.5 kcal/mol; see the Supporting Information for the full list of energies. Thus there is only an insignificant effect of the above structural issue on the final reaction energy profile. The above comparison is in line with a wealth of experience indicating that the relative energetics is very insensitive to details of the geometries.[61,45] In the case of manganese catalase internuclear distance improvements of 0.05−0.10 Å led to changes of the relative energies of only a few tenths of a kcal/mol.[61]

Table 3. Ni−Ligand Bond Lengths (Å) for Various Model States (Nonprime, Prime, Double-Prime, Transition States) Discussed in the Text[a]

	axial ligands		equatorial ligands			
state	Ni–O[b]	$Ni-N^{\delta}_{His1}$	$Ni-S_{Cys2}$	$Ni-S_{Cys6}$	$Ni-N_{Cys2}$	$Ni-N_{His1}$
$\mathbf{1}^2$	−	2.07	2.28	2.32	1.95	2.04
$\mathbf{2}^3$	2.15	2.10	2.34	2.37	1.95	2.04
$\mathbf{3}^1$	2.02	2.05	2.65[d]	2.42	2.00	2.11
$\mathbf{4}^3$	−	2.06	2.60[d]	2.37	2.03	2.12
$\mathbf{5}^2$	1.97	2.03	2.64[d]	2.40	1.99	2.11
$\mathbf{6}^2$	2.34	2.10	2.33	2.39	1.94	2.05
$\mathbf{3'}^3$	2.09	−	2.27[d]	2.32	1.93	2.03
$\mathbf{4'}^1$	−	−	2.25[d]	2.31	1.91	1.98
$\mathbf{5'}^2$	2.01	−	2.30[d]	2.34	1.94	2.03
$\mathbf{1''}^2$	−	−	2.26	2.21	1.86	2.00
$\mathbf{2''}^3$	2.02	−	2.29	2.36	1.88	2.01
$\mathbf{3''}^3$	2.01	−	2.41[d]	2.31	1.92	1.98
$\mathbf{4''}^1$	−	−	2.33[d]	2.28	1.91	1.94
$\mathbf{5''}^2$	2.00	−	2.43[d]	2.33	1.92	1.99
$\mathbf{6''}^2$	2.10	−	2.26	2.35	1.92	2.03
$\mathbf{TS1}^3$	2.10	2.10	2.40	2.37	1.95	2.05
$\mathbf{TS2}^2$	2.02	2.04	2.68	2.43	1.98	2.08
$\mathbf{TS3}^3$	2.05/2.17[c]	−	2.33	2.34	1.95	2.08
$\mathbf{TS4}^3$	−	−	2.45	2.29	1.99	2.11
$\mathbf{TS4}^3$	−	−	2.45	2.29	1.99	2.11
$\mathbf{TS5}^2$	1.95	−	2.38	2.33	1.94	2.05

[a] In cases when the corresponding coordination site is empty, the data are absent. For a given state, only its most stable spin configuration data are given. [b] The substrate derived oxygen atom. [c] Bidentate superoxide coordination was obtained for this state. [d] These values for **3**−**5** states correspond to the protonated S_{Cys2} ligand.

III.g. Reaction Energetics. Redox potentials for reactants vs products ($E^{o\prime}(O_2/O_2^{\bullet-})$ = −0.16 V and $E^{o\prime}(O_2^{\bullet-}/H_2O_2)$ = +0.89 V) of the dismutation reaction in eq 1 give a total reaction

(55) Fee, J. A.; DiCorleto, P. E. *Biochemistry* **1973**, *12*, 4893−4899.
(56) Lawrence, G. D.; Sawyer, D. T. *Biochemistry* **1979**, *18*, 3045−3050.
(57) St. Clair, C. S.; Gray, H. B.; Valentine, J. S. *Inorg. Chem.* **1992**, *31*, 925−927.
(58) Azab, H. A.; Banci, L.; Borsari, M.; Luchinat, C.; Sola, M.; Viezzoli, M. S. *Inorg. Chem.* **1992**, *31*, 4649−4655.
(59) Verhagen, M. F.; Meussen, E. T.; Hagen, W. R. *Biochim. Biophys. Acta* **1995**, *1244*, 99−103.
(60) Allen, F. H. *Acta Crystollagr. B* **2002**, *58*, 380−388.
(61) Siegbahn, P. E. M. J. *Comput. Chem.* **2001**, *22*, 1634−1645.

energy of −24.2 kcal/mol according to eq 14. This is in a very good agreement with the currently obtained value of −7.0 − 17.0 = −24.0 kcal/mol summing over the reductive and oxidative half-reactions. This agreement merely shows that the presently applied energy correction of 3.0 kcal/mol is a good estimate for the $O_2^{\bullet-}$ protonation in solution; see section II. The overall energetics includes no influence from the Ni redox properties: states **1**[2] (the resting Ni(III) enzyme) and **4**[3] (the intermediate Ni(II) between the two half-reactions) cancel out when considering the full reaction cycle. Only the individual half-reaction energies allow a prediction of the Ni coupled redox potential $E^{\circ\prime}$(Ni(III/II)) = 0.14−0.15 V, relevant for the catalytic process. This value is within the redox potential range experimentally obtained for CuZnSOD, $E^{\circ\prime}$(Cu(II/I)) = 0.12−0.42 V,[55−59] and closely approaches the values for FeSOD, $E^{\circ\prime}$(Fe(III/II)) = 0.25 V,[62] and MnSOD, $E^{\circ\prime}$(Mn(III/II)) = 0.31−0.40 V[63] (the MnSOD coupled redox potential was derived from the reaction kinetics[64,65]). While the experimental data on the NiSOD redox potential are missing, the presently obtained data suggest that the metal ligand field in NiSOD with the two Cys2 and Cys6 thiolates indeed noticeably lowers the $E^{\circ\prime}$(Ni(III/II)), expected to be ∼1 V for O/N ligand coordination.

IV. Conclusions

The present DFT study focuses on exploration of the potential energy surface of the NiSOD reaction mechanism. Over 30 different states (counting local minima and transition states, and considering the proton location and spin alternatives) of the active site model were analyzed. An accurate description of spin crossovers, common in transition metal chemistry, was presently omitted. The singlet−triplet spin transitions were merely ad hoc considered above. In view of the recent theoretical study on CuZnSOD,[54] an important assumption currently made is that superoxides and protons are concomitantly delivered to the active site as a neutral ·OOH hydroperoxyl radical. This concerted delivery scheme applies to both the reductive and oxidative half-reactions. The correction to the relative energies of 3.0 kcal/mol (see sections II and III.b) is made considering that the $O_2^{\bullet-}$ superoxide radical is unprotonated at pH = 7. Consistent with the observed rapid decrease of the NiSOD activity at higher alkaline pH's above 8,[9,13] the correction energy will increase with pH.

The NiSOD dismutation scenario obtained has characteristic features very similar to the recently studied mechanism of CuZnSOD:[54] (*i*) the redox processes (**3** → **4** + $\mathbf{O}_2$ and **4** + $\mathbf{O}_2^{\bullet-}$ → **5**[2] here) are spontaneous, and (*ii*) the only transition states involve proton transfer between the inbound substrate and a group, present in the enzyme active site. This group accepts the proton during the reductive phase allowing for O_2 release, hosts the proton in the reduced state, and donates the proton back allowing for H_2O_2 release during the oxidative phase. Additionally, (*iii*) the substrate binding is favorable only in the oxidative phase, and this oxidative binding results in the only stable minimum **5** on the profile. The rest of the intermediates (**2**, **3**, and **6** here) are metastable when considering the accurate Gibbs free energies. For NiSOD, the substrate binding in **5** is nearly thermoneutral (0.6 kcal/mol only), and therefore existence of intermediates can be argued for the entire dismutation reaction. Notably, the absence of the intermediates can be interpreted in favor of the outer-sphere electron transfer mechanism, where superoxide approaches closely to the Ni center but does not actually coordinate to it.

The most likely group to host the proton between the reductive and oxidative phases is the S^-_{Cys2} thiolate sulfur. N^{δ}_{His1} of His1 imidazole and backbone amides of the residues forming the active site walls can be considered as states lying outside the normal reaction pathway. Notably, protonation of N^{δ}_{His1} was observed only in the chemically or X-ray-reduced NiSOD, which led to mechanistic proposals analogous to CuZnSOD as in eqs 2 and 3. The present scenario favors that the Ni−N^{δ}_{His1} axial coordination remains intact throughout the catalytic cycle. The main role for the His1 axial ligand in the present mechanism is the indirect influence on the Ni(III) S^-_{Cys2} thiolate ligand, allowing for its facile protonation as in eqs 4 and 5 (see the discussion on double-prime states relative energies in section III.c).

Among alternative reaction mechanisms, the reductive phase was shown (see section III.e) to proceed without an extra proton as well. Starting from the Ni(III)−$O_2^{\bullet-}$ complex **3**$^-$, O_2 release coupled to the metal reduction is a favorable entropy-driven process.

Acknowledgment. The National Supercomputer Center (NSC) in Linköping is gratefully acknowledged for a generous grant of computer time. We thank Louis Noodleman for valuable discussions and Sven de Marothy for use of XYZ-Viewer program.

Supporting Information Available: GIF files showing imaginary vibrations for the transition states **TS1** and **TS2**; XYZ format coordinates (B3LYP/LACVP) and Ni−ligand distances (B3LYP/LACVP and PW91/LACVP*) for the various model states discussed in the text (only the most stable spin configurations are given); accurate B3LYP/LACV3P** energies for the B3LYP/LACVP and PW91/LACVP* optimized structures; complete list of authors for ref 40. This material is available free of charge via the Internet at http://pubs.acs.org.

JA053665F

(62) Vance, C. K.; Miller, A.-F. *J. Am. Chem. Soc.* **1998**, *120*, 461.
(63) Han, W.-G.; Lovell, T.; Noodleman, L. *Inorg. Chem.* **2002**, *41*, 205−218.
(64) Bull, C.; Niederhoffer, E. C.; Yoshida, T.; Fee, J. A. *J. Am. Chem. Soc.* **1991**, *113*, 4069.
(65) Hsu, J.-L.; Hsieh, Y.; Tu, C.; O'Connor, D.; Nick, H. S.; Silverman, D. N. *J. Biol. Chem.* **1996**, *271*, 17687.